Journal of Power Sources 546 (2022) 231988

Contents lists available at ScienceDirect

Journal of Power Sources

journal homepage: www.elsevier.com/locate/jpowsour

Sulfur-doped carbon nanofibers as support for tantalum oxides bifunctional catalysts for the oxygen reduction and evolution reactions

Juan Carlos Ruiz-Cornejo [a], David Sebastián [a,*], Juan Ignacio Pardo [b], María Victoria Martínez-Huerta [c], María Jesús Lázaro [a,**]

[a] Instituto de Carboquímica, CSIC. Miguel Luesma Castán 4, 50018, Zaragoza, Spain
[b] Group of Applied Thermodynamics and Surfaces (GATHERS), Aragon Institute for Engineering Research (I3A), Universidad de Zaragoza, EINA, 50018, Zaragoza, Spain
[c] Instituto de Catálisis y Petroleoquímica, CSIC, Marie Curie 2, 28049, Madrid, Spain

HIGHLIGHTS

- Carbon nanofibers are doped with sulfur (1.6–1.8 at.% XPS).
- Sulfur-doped carbon nanofibers are studied as support for tantalum oxides.
- The sulfur doping significantly improves ORR activity.
- Improved OER/ORR bifunctional activity upon doping.
- Good catalyst durability after OER/ORR galvanostatic cycles.

ARTICLE INFO

Keywords:
Sulfur-doped carbon nanofibers
Tantalum oxide
Bifunctional electrocatalyst
Oxygen evolution reaction
Oxygen reduction reaction

ABSTRACT

Highly efficient, low-cost and stable bifunctional catalysts for oxygen reduction reaction (ORR) and oxygen evolution reaction (OER) are highly desirable for the development of green electrochemical energy storage and conversion devices. Here, we report the synthesis of sulfur-doped carbon nanofibers (CNF) as support for tantalum oxide nanoparticles. Carbon nanofibers and tantalum oxides represent a durable choice for oxygen electrocatalysis, but an improvement of catalytic activity is required. Upon doping, sulfur is found to be mainly bonded to carbon as C–S–C species (more than 80%). The results show that the effective incorporation of sulfur in the support has a clear positive effect on the electroactivity of the tantalum oxide catalysts. It causes a decrease of OER/ORR overpotential of 80 mV with respect to the undoped counterpart, with special improvement in the ORR. The new catalysts have shown an interesting bifunctional behavior for the OER and ORR, as well as a good stability through time.

1. Introduction

The design of efficient electrocatalytic materials for the development of green electrochemical energy storage and conversion devices, such as unitized regenerative fuel cells or rechargeable metal-air batteries, has become a promising way to solve the global energy demand and the environmental-related problems. However, the commercial applications are severely hampered by the high cost and poor stability of the bifunctional catalysts for oxygen reduction reaction (ORR) and oxygen evolution reaction (OER) [1–4].

Carbon-based materials have been studied in the last decades for their use as electrocatalysts for oxygen reduction and evolution reactions due to their good electrochemical properties such as high conductivity and catalytic activity. However, their main shortcoming is related to the weak resistance to corrosion and oxidation of carbon materials during OER, which restricts their use as bifunctional oxygen catalysts. To solve this issue, advanced carbon nanostructures, such as graphene, carbon nanofibers or carbon nanotubes, have shown promising performance and stability as bifunctional catalysts [5–7]. Among them, one dimensional carbon materials like carbon nanofibers (CNFs)

* Corresponding author.
** Corresponding author.
E-mail addresses: dsebastian@icb.csic.es (D. Sebastián), mlazaro@icb.csic.es (M.J. Lázaro).

https://doi.org/10.1016/j.jpowsour.2022.231988
Received 27 April 2022; Received in revised form 12 August 2022; Accepted 14 August 2022
Available online 24 August 2022

have shown great potential because of their graphite-like structure together with more exposed active sites [8]. Therefore, CNFs contribute to increase the electrical conductivity, improve the resistance to corrosion processes and help to the diffusion of reagents and products [9–14].

One of the most relevant properties of carbon materials in increasing activity is the presence of heteroatoms at the surface, such as N, S and P. The insertion of heteroatoms into sp^2-hybridised carbon structures has been proven to be an effective way of modifying their electrical properties, chemical activity and stability [15–20]. Among heteroatoms, nitrogen has been extensively investigated for fuel cells and bifunctional catalysts [21,22], including those based on carbon nanofibers [23–26], but sulfur is gaining increasing attention due to the interesting electrochemical properties generated on sulfur-doped carbons. Higgins et al. developed a sulfur-doped graphene supported Pt-based catalyst with excellent activity for the ORR [27]. They reported that the presence of sulfur led to stronger adsorptive and cohesive binding energies with Pt nanoparticles, providing both beneficial catalytic activity and stability enhancements. Pt/S-Graphene provided 139 mA mg^{-1}Pt at 0.9 V vs. RHE, better than commercial Pt/C (121 mA mg^{-1}Pt) and Pt/Graphene (101 mA·mg^{-1}Pt). Hoque et al. designed Pt nanowires/sulfur doped graphene as ORR catalysts in acidic electrolyte. The amount of sulfur significantly affected the ORR kinetics of the Pt nanowires. They got 182 mA·mg^{-1}Pt at 0.9 V vs. RHE at a content of 1.4 wt% sulfur [28,29]. Li et al. enhanced the electrocatalytic stability of Pt supported on sulfur doped pristine carbon for the ORR in 0.1 M KOH using *in-situ* solution plasma with a sulfur content of 4 wt% [30]. However, bifunctional electrocatalysts based on sulfur-doped carbons have been less investigated for both oxygen evolution and reduction reactions [6,31,32]. Gao et al. synthesized manganese oxide/sulfur-doped graphitized carbon as bifunctional catalyst for ORR/OER. The current density reached −3 mA cm^{-2} at 0.81 V vs. RHE (for ORR) and 10 mA cm^{-2} at 1.62 V vs RHE (for OER) in 0.1 M KOH [32]. El-Sawy et al. incorporated heterocyclic sulfur into the carbon nanotube-graphene structure by a bidoping strategy, which not only enhanced OER activity with an overpotential of 0.35 V at a current density of 10 mA cm^{-2}, but also retained 100% of stability after 75 h. Furthermore, the sulfur-doped carbon showed high catalytic activity for the ORR [6].

In previous works, we investigated a microemulsion procedure to create tantalum based catalysts [33], and carbon nanofibers as support for such tantalum-based nanoparticles, which demonstrated to be active and durable for OER [34]. Oxides from metals of groups 4 and 5 of the periodic table are known as highly durable catalysts, which combined with CNFs, represent a good opportunity towards durable and active bifunctional oxygen catalysts. In this work, we seek an enhancement of electroactivity by doping the CNF support with sulfur. We report the preparation of tantalum oxides supported on different sulfur-doped carbon nanofibers obtained by varying the temperature and duration time of the doping process. These materials were investigated as bifunctional catalysts for ORR and OER in alkaline medium. Physical and chemical properties of the supports as well as the corresponding bifunctional catalysts were characterized using several techniques. The electrocatalytic performance for ORR/OER was assessed using a rotating ring-disk electrode and the stability through time of these new materials was evaluated.

2. Experimental

2.1. Synthesis of tantalum-based electrocatalysts

2.1.1. Synthesis of CNF

The catalyst for CNF synthesis, composed by Ni–Cu–Al_2O_3 (Ni:Cu:Al molar ratio of 78:6:16), was prepared by coprecipitation of metal nitrates ($Ni(NO_3)_2{\cdot}6H_2O$, $Cu(NO_3)_2{\cdot}3H_2O$ and $Al(NO_3)_3{\cdot}9H_2O$, Sigma-Aldrich, > 99%), followed by calcination (air) at 450 °C for 8 h and subsequent reduction in hydrogen (Messer, > 99.5%) at 550 °C for 1 h. The catalyst composition and preparation correspond to previous investigation showing high methane conversion and stability [35]. For the growth of CNFs, 300 mg of the Ni-based catalyst was placed into a vertical fixed bed reactor under nitrogen flow (Messer, > 99.8%) and heated up to 700 °C. Then, methane (Air Products, 99.995%) was fed to the catalyst sample for 620 min at ambient pressure. The reactor was then cooled to room temperature under inert atmosphere (N_2). Finally, CNFs were washed with 0.1 M $HClO_4$ aqueous solution at 60 °C for 15 min in order to eliminate the nickel used for the growing process, followed by thorough washing with deionized water and drying at 60 °C overnight.

2.1.2. Sulfur doping of CNF

CNF was mixed with elemental sulfur powder (Alfa Aesar), with a mass ratio of 95:5 (carbon:sulfur), in an agate mortar and deposited in a ceramic boat. The mixture was introduced in a horizontal reactor and thermally treated under inert atmosphere (N_2). Two procedures were used to dope the CNF. One of them consisted of treating the sample at 250 °C for 6 h and the other one at 400 °C for 3 h, in both cases the heating rate was 5 °C min^{-1}. As-prepared samples were washed with carbon disulfide (99.5%, Panreac) to eliminate the non-doping sulfur in the material, rinsed with ethanol, then with water, filtered, and finally dried in an oven at 60 °C. The sulfur-doped CNFs were labeled as CNF-SX where X stands for the CNF doping temperature (250 or 400 °C).

2.1.3. Synthesis of tantalum-based electrocatalysts

Tantalum-based oxides (general formula TaO_x) were deposited on the sulfur doped CNF by a microemulsion procedure [34]. The microemulsion (ME) consisted of mixing 0.25 mL of 75 mM NaOH aqueous solution (Alfa Aesar, 99.99%) with an oil phase composed of 2.3 g of surfactant (Igepal CO-520, Aldrich), 20 mL of n-heptane (Honeywell) and 0.75 mL of ethanol (Labkem, 99.5%). Then 0.05 mL (0.3 mmol) of tantalum (V) ethoxide (Aldrich, 99.98%) was added to the ME under continuous stirring at room temperature. According to previous works, the mixture reacts producing tantalum oxide nanoparticles within 5 min [36]. Afterwards, 312 mg of the S-doped CNF was added to the suspension and stirred overnight. The two doped CNF described in the previous section were used as supports, as well as undoped CNF for comparison purposes. In the next step, the materials were washed with ethanol and then with water, followed by drying at 60 °C overnight. The final step consisted of a heat treatment in inert atmosphere (N_2) for 90 min at 900 °C. Finally, the material was washed with deionized water and dried at 60 °C overnight. The catalysts were labeled as TaO_x/CNF–S250 and TaO_x/CNF–S400.

2.2. Solid-state characterization

The concentration of nickel and tantalum was determined by inductively coupled plasma atomic emission spectroscopy (ICP-OES) using a Xpectroblue-EOP-TI FMT26 (Spectro). The weight percentages of sulfur and carbon were obtained by elemental analysis in a Thermo Flash 1112 equipment.

Nitrogen physisorption experiments were carried out in a Quantachrome equipment and analyzed with Quadrawin software. Adsorption-desorption isotherms were obtained at −196 °C. Brunauer-Emmet-Teller equation was used to calculate the BET specific surface area and the Barret-Joyner-Halenda model, applied to the desorption branch of the isotherms, was considered to determine the pore size distribution.

X-ray photoelectron spectroscopy (XPS) was used in order to determine the concentration of species and the oxidation state of the doping sulfur and tantalum. The analyses were carried out in an ESCA+ (Omicron) and analyzed using CasaXPS software.

The X-ray diffraction (XRD) analyses were obtained in a Brucker D8 Advance diffractometer with CuKα radiation of 1600 W. The diffractograms were analyzed using TOPAS and EVA software and compared to the patterns of the different phases from the International Center for

Diffraction Data (ICDD).

Transmission electron microscopy (TEM) pictures were taken in a Tecnai F30 (FEI) microscope. For this purpose, the electrocatalysts were dispersed in ethanol and dropped on a carbon film coated Cu grid. For each catalyst, the particle size distribution of the deposited tantalum oxides was calculated using ImageJ software on TEM images and then analyzed with the statistic tools of OriginLab software.

The ratio between oxygen and tantalum was determined with a Scanning Electron Microscopy-Energy Dispersive X-ray spectroscopy (SEM-EDX) SEM-EDX Hitachi S-3400 N with EDX Röntec XFlash of Si (Li).

2.3. Electrochemical characterization

Electrochemical analyses were carried out in a three-electrode cell at room temperature using a 0.1 M NaOH aqueous solution as electrolyte (NaOH 99.99%, Alfa Aesar), prepared with ultrapure water (Milli-Q, 18.2 MΩ cm). For ORR experiments, the NaOH solution was saturated with O_2 (Messer, 99.5%). The reference electrode was a reversible hydrogen electrode (RHE) and the counter electrode a glassy carbon rod. The catalysts were placed on a rotating ring-disk electrode (RRDE) composed of a glassy carbon disk (5 mm diameter) and a Pt ring. The catalytic layer was made using 1 mg mL^{-1} ink obtained by sonicating the catalyst in isopropanol/water (50:50) and Nafion® (30 wt% of the catalytic layer), which acted as a binder. The required drops of ink were located onto the glassy carbon disk to get the needed mass loading. The catalyst loading on the disk was estimated to be 500 μg cm^{-2}. The study of the ORR was performed by linear sweep voltammetry (LSV) from 1.0 to 0.3 V vs. RHE and at a scan rate of 5 mV s^{-1} with varying rotating speeds from 400 to 1600 rpm. The study of the OER was performed between 1.0 and 1.9 V vs. RHE and at a scan rate of 5 mV s^{-1} with a rotating speed of 1600 rpm to ease the diffusion of evolved oxygen.

The percentage of H_2O_2 formation during the ORR experiments was calculated according to **Equation (1)**, with j_r = current at the ring (at constant potential of 1.2 V vs. RHE), j_d = current at the disk and N = 0.249 (collection efficiency).

$$\%H_2O_2 = 100 \cdot \frac{2 \cdot j_r}{N \cdot j_d + j_r} \quad (1)$$

The kinetic current density in the ORR, j_k, was calculated by **Equation (2)** considering that the measured current density, j, can be expressed as the separate contribution from j_k and the diffusion limiting current density, j_{lim}, as follows:

$$\frac{1}{j} = \frac{1}{j_k} + \frac{1}{j_{lim}} \quad (2)$$

The oxygen efficiency in the OER, ε, this is the percentage of current actually transformed in oxygen, was calculated according to **Equation (3)**, where N, j_r and j_d stand again for the collection efficiency, current at the ring (at 0.6 V vs. RHE) and current at the disk, respectively, whereas n_{ORR} is the number of electrons for the reduction at the ring of the oxygen evolved from the disk (for Pt ring, $n_{ORR} = 4$).

$$\varepsilon\ (\%) = 100 \cdot \frac{\frac{4}{n_{ORR}} \cdot j_r}{N \cdot j_d} \quad (3)$$

Tafel slopes (b) for both ORR and OER were determined upon ohmic resistance correction (iR correction) of potential values. For this, the ohmic resistance was estimated from Newman's equation to be 8 Ω cm^2. **Equation (4)** describes the correlation of current (j_k for ORR and j for OER) and iR-corrected potential ($E_{iR\text{-}free}$), with Tafel slope (b), exchange current density (j_0) and reversible potential (E^0 = 1.23 V vs. RHE):

$$\eta = \left| E_{iR-free} - E^0 \right| = b \cdot log\left(\frac{j}{j_0}\right) \quad (4)$$

Endurance tests were done to determine the variation of the behavior of the catalysts over time. For this purpose, chronopotentiometric tests were carried out, consisting of consecutive square cycles alternating either a positive or negative current density of 1 mA cm^{-2} maintained for 180 s. Cut-off potentials of 1.9 V and 0.2 V vs. RHE were established. These tests were also done on a three-electrode cell with the same characteristics as those previously described, but now using a rotating disk electrode (RDE), with a glassy carbon tip of 5 mm and working at a rotating speed of 400 rpm.

3. Results and discussion

3.1. Physico-chemical characterization

The chemical composition of the electrocatalysts was studied by elemental analysis, ICP-OES, SEM-EDX and XPS (see Tables 1 and 2). The weight percentage of sulfur for the two doped supports is similar with slightly higher concentration for the sample treated at 400 °C, as observed from elemental analysis and EDX results. The content of sulfur decreases slightly after introducing the tantalum-based catalytic particles (Table 1), most probably because of the increase of the relative content of tantalum species, which is consistent with the decrease of carbon concentration. With regard to the metallic phase, ICP analysis showed less content of Ta for S-doped CNF catalysts than for the undoped one following the same synthesis procedure (Table 2) [34]. The porous structure of supports was evaluated by nitrogen physisorption. The adsorption/desorption isotherms as well as the pore size distribution are included in the supplementary information (Fig. S1). The incorporation of sulfur species did not significantly alter the porous structure of the filaments, with similar values of both BET and external surface area (in between 55 and 70 m^2 g^{-1}, Table S1), a pore volume between 0.22 and 0.32 cm^3 g^{-1}, and a negligible content of micropores, as expected for this kind of materials [10]. The different content of Ta on supports with similar porosity indicates that the anchorage of tantalum nanoparticles is less efficient when there are sulfur species on the surface of carbon nanofibers. By comparison of the two S-doped TaOx catalysts, ICP analyses evidence a larger concentration of Ta on the support doped at 250 °C whereas XPS indicates a larger amount of Ta on the one doped at 400 °C. From this point of view, the CNF doped at 400 °C (CNF–S400) clearly favors the presence of tantalum particles on the surface compared to CNF–S250. The difference could be associated to the chemical speciation of sulfur, as discussed next. ICP results also evidenced the presence of nickel (1.8–2.6 wt%) even after the acid leaching of the samples. Interestingly, nickel was not detected in XPS analyses, most probably because it is encapsulated by carbon inside the CNF.

A relevant parameter is the oxygen/tantalum atomic ratio, which is summarized in Table 2 from EDX and XPS analyses. The determination of the composition of the tantalum oxides by SEM-EDX was done by selecting areas with metal oxide nanoparticles, with the idea of minimizing the carbon and oxygen peaks from the supporting materials. The oxygen vacancies/substoichiometry has been correlated to favor the electrochemical activity for oxygen related reactions in oxides of metals from groups 4 and 5 [37]. In our case, Both EDX and XPS results do not

Table 1
Bulk and surface composition of the TaO_x catalysts and supports obtained by elemental analysis and XPS, respectively.

Sample	Elemental analysis		XPS				EDX
	C wt. %	S wt. %	C at. %	O at. %	S at. %	Ta at. %	S at. %
CNF–S250	95.5	1.1	94.7	3.67	1.60	–	0.54
CNF–S400	95.5	1.3	95.1	3.09	1.79	–	0.80
TaOx/ CNF–S250	75.5	1.0	95.7	2.41	1.46	0.41	0.43
TaOx/ CNF–S400	84.0	0.9	94.8	2.86	1.15	1.23	0.42

Table 2
Tantalum and nickel content in the catalysts as determined by ICP and XPS and O/Ta atomic ratio by SEM-EDX and XPS.

Catalyst	ICP		XPS	EDX	XPS
	Ni wt.%	Ta wt.%	Ta wt.%	O/Ta	O/Ta
TaOx/CNF–S250	2.6	10.0	5.4	4.1	5.8
TaOx/CNF–S400	2.3	6.3	15.3	3.6	2.3
TaOx/CNF[a]	1.8	20.5	14.1	2.9	3.5

[a] Catalyst synthesized under the same conditions on undoped CNF.

indicate a ratio below the stoichiometric one for the most abundant phase (O/Ta = 2.5 for Ta_2O_5), but it must be considered that the support itself provides around 3 at.% oxygen (Table 1). Only in the case of TaOx/CNF–S400 the XPS analysis indicates O/Ta below 2.5, which points to a larger substoichiometry in this catalyst compared to the other formulations.

XPS analyses also show the different speciation of sulfur in the most external surface of the doped CNFs, as represented in Fig. 1. Regarding the supports (Fig. 1a), the S2p$_{3/2}$ signal point out the presence of two

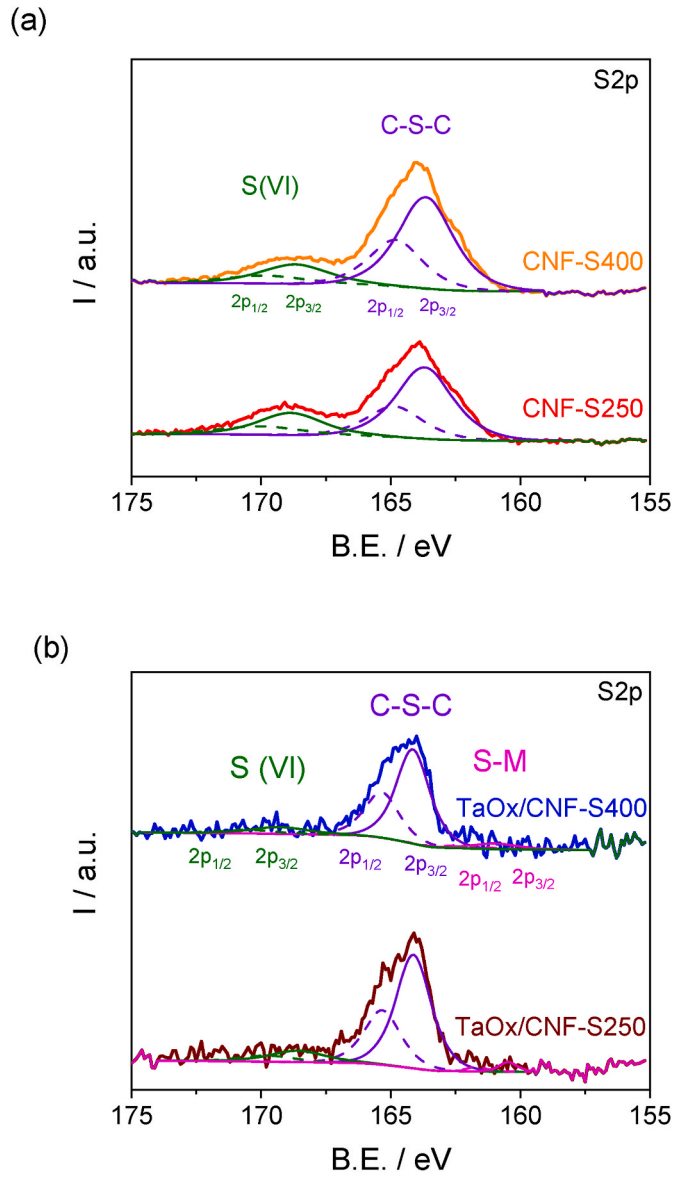

Fig. 1. XPS deconvoluted signals for S2p of (a) sulfur doped CNF: CNF–S250 and CNF–S400; and (b) the catalysts TaOx/CNF–S250 and TaOx/CNF–S400.

main peaks at binding energies close to 164 eV and 169 eV, corresponding to two different oxidation states of sulfur: C–S–C and sulfoxide (S VI), respectively. The proportion of each functional group for each support is show in Table 3, indicating a larger content of C–S–C in the CNF doped at higher temperature (400 °C). This difference may partially explain the higher concentration of tantalum at the surface for TaOx/CNF–S400 discussed before. Sulfur doped carbon materials are known for their capacity to adsorb metals, e.g. for decontamination purposes [38]. Since the main difference between our two S-doped supports is sulfur speciation, the enrichment of tantalum at the surface for TaOx/CNF–S400 could be related to more sulfur bonded to carbon. Interestingly, after tantalum is incorporated on the support, sulfur appears mainly as C–S–C, with 83–85% as shown in Table 3 and Fig. 1b. In the catalysts, there is also a small contribution of sulfur bonded to metal appearing at lower binding energy of 162 eV (S-M), most probably nickel sulphide as identified in XRD analyses.

XPS analyses revealed a different Ta concentration at the most external surface of each catalyst. The Ta 4f signal for the catalysts is showed in Fig. 2. The signal with a binding energy close to 27 eV, which corresponds to Ta 4f$_{7/2}$, indicates the presence of Ta (V) oxidation state [39].

XRD diffractograms for the S-doped and undoped catalysts are found in Fig. 3. Different phases were detected in the different materials: carbon, nickel and nickel sulphides (Ni_3S_2, NiS_2, NiS) from the support (see supplementary information, Fig. S2, Table S2 and Table S3), and up to three phases containing Ta oxides (Ta_2O_5, TaO and $NaTaO_3$). Regarding the support-related species, the S-doped supports without Ta oxides contain both NiS_2 (major) and NiS. Interestingly, the catalysts reveal that nickel sulphides have been completely converted to the nonstoichiometric Ni_3S_2 upon thermal treatment.

With regard to the tantalum related phases, the major contribution to XRD reflections comes from Ta_2O_5, with a minor contribution of TaO (in particular for TaOx/CNF–S250) and even lower signal associated to $NaTaO_3$, only for the undoped catalyst. It must be said that the presence of a mix of tantalum oxide species has been recently reported to tailor surface behavior by creating a charge transfer accumulation at their interface, caused by significant changes in the work function of the tantalum species, which results in enhanced electrocatalytic behavior [40].

To delve into the crystallinity of the catalysts, XRD patterns were analyzed with Topas software (Lebail method) and the lattice parameters calculated from XRD for the CNF-supported TaO_x electrocatalysts are summarized in Table 4, whilst the crystallite sizes are gathered in Table 5. It is interesting to mention that the lattice parameters for Ta_2O_5 are slightly lower compared to the reference pattern (JCPDS#89–2843) with stoichiometric formula. This is more evident in peaks (0 0 1) and (0 0 2) of Ta_2O_5, which appear about 0.2–0.3° shifted to higher Bragg angles (2θ) compared to the ICDD reference (JCPDS#89–2843). The contraction of the unit cell, together with chemical composition discussed before, could be associated to oxygen deficiency, as stated in previous works [33,34,41].

TEM and STEM images were evaluated in order to study the

Table 3
Chemical speciation of sulfur as obtained by the deconvolution of S2p XPS signal.

Sample	S 2p Total at. %	S-M (161 eV, 2p$_{3/2}$) %	C–S–C (163.6 eV, 2p$_{3/2}$) %	S (VI) (168.8 eV, 2p$_{3/2}$) %
CNFS 250	1.60	–	48	52
CNFS 400	1.79	–	64	36
TaOx/ CNF–S250	1.46	4	83	13
TaOx/ CNF–S400	1.15	6	85	9

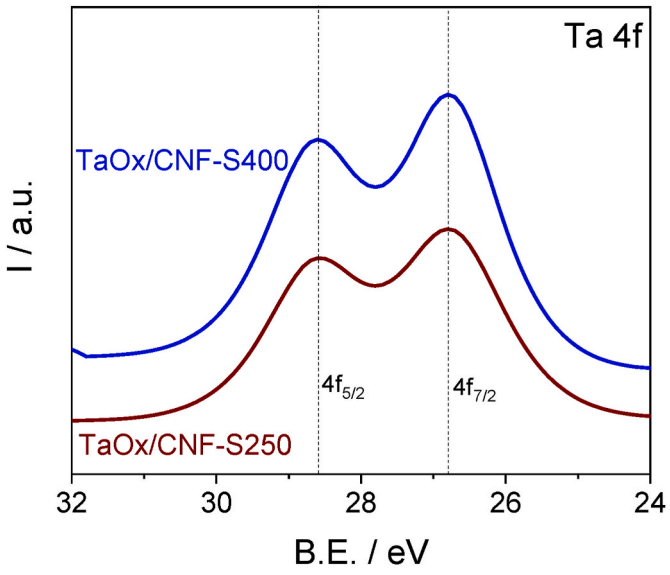

Fig. 2. XPS signals for Ta 4f of the sulfur-doped CNF-supported TaOx catalysts.

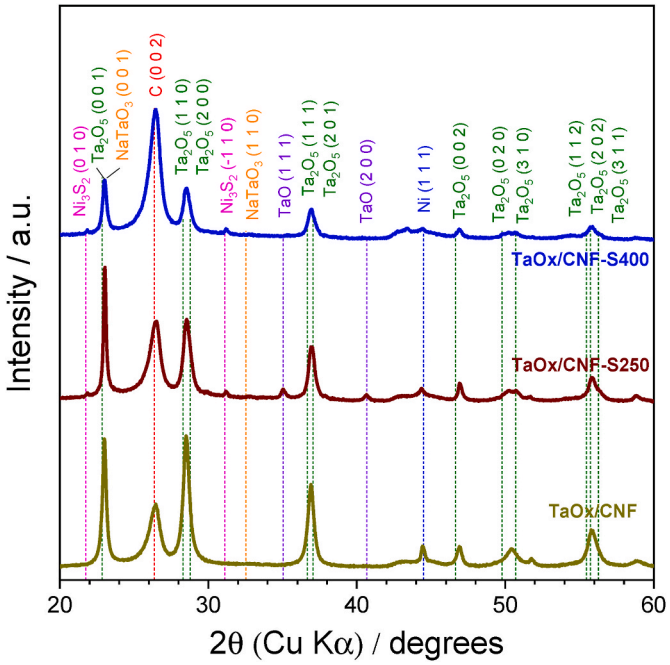

Fig. 3. XRD diffractograms for the electrocatalysts. Vertical lines indicate the position for main reflections according to International Center for Diffraction Data (ICDD) values (Ta_2O_5 JCPDS#89–2843, TaO JCPDS#89–4772, $NaTaO_3$ JCPDS#74–2477, C JCPDS#41–1487, Ni JCPDS#87–0712, Ni_3S_2 JCPDS#85–1802).

morphology of S-doped CNF-supported TaOx catalysts. Some images are collected in Fig. 4. Both electrocatalysts are composed of carbon nanofibers with tantalum-based particles on their surface. The metal oxide nanoparticles are distinguished from the filaments by darker contrast in TEM images (left side of figure) and by lighter contrast in STEM images (right side of figure).

The particle size distributions of the tantalum particles are depicted in Fig. 5 for both catalytic materials from TEM images. The main difference is that TaOx/CNF–S250 shows a broader distribution and particles with bigger size than TaOx/CNF–S400. The average particle size is 24.1 ± 6 nm for TaOx/CNF–S250, and 13.6 ± 3 nm for TaOx/CNF–S400, in line with crystallite sizes reported in Table 5 for Ta_2O_5 from XRD results (23.5 and 17.8 nm, respectively).

3.2. Electrochemical characterization

3.2.1. ORR Electro-activity of S-doped CNF-supported Ta-based catalysts

The electrochemical ORR activity in alkaline electrolyte for the different catalysts is depicted in Fig. 6. The disk current density (Fig. 6a) presents a sigmoidal wave form, as typically occurs for the oxygen electroreduction with oxygen saturated in the electrolyte, reaching a limiting current density at high overpotential attributed to oxygen diffusion limitation. First, by comparing the ORR activity of CNF–S250 and CNF–S400 with the catalysts TaOx/CNF–S250 and TaOx/CNF–S400, it is clear that the addition of tantalum oxides has a positive effect on the activity, with a potential shift of about 40 mV for TaOx/CNF–S250 and 60 mV for TaOx/CNF–S400, in terms of half-wave potential. This comparative study is useful to discard the eventual effect of nickel on ORR activity over the effect of tantalum oxides. There is a clear positive effect of tantalum oxide phases on the electroactivity regardless the presence of nickel traces.

On the other hand, by comparison with the undoped support (TaOx/CNF), the introduction of sulfur has also a significantly positive effect on the ORR activity of doped catalysts, with more than 50 mV enhancement. The S-doped TaOx catalysts present a small amount of Ni_3S_2, as discussed from XRD characterization. A certain contribution of this phase to the activity cannot be discarded, even if nickel sulfide is at the level of traces.

Fig. 6b depicts the ring current at 1.2 V vs. RHE for the three TaOx catalysts, which is attributed to the oxidation of the hydrogen peroxide evolved at the disk. In the inset of Fig. 6b the evolution of H_2O_2 percentage with potential is shown, with about 50% average production. This indicates a number of electrons close to 3. There are no significant

Table 5
Crystallite sizes (nm) of tantalum- and nickel-related phases identified from XRD analyses for the CNF-supported TaOx electrocatalysts.

Catalyst	Ta_2O_5 (nm)	TaO (nm)	$NaTaO_3$ (nm)	Ni (nm)	Ni_3S_2 (nm)
TaOx/CNF–S250	23.5	31.2	–	19.1	8.5
TaOx/CNF–S400	17.8	–	–	3.2	8.2
TaOx/CNF	16.0	38.3	30.9	38.9	–

Table 4
Lattice parameters obtained from XRD for the TaOx/CNF electrocatalysts.

Phase	Ta_2O_5			TaO	$NaTaO_3$			
System (space group) ICDD card number	Orthorombic (C2mm) PDF 89–2843			Cubic (Fm-3m) PDF 89–4772	Monoclinic (P2/m) PDF 74–2477			
Lattice parameter	a/Å	b/Å	c/Å	a/Å	a/Å	b/Å	c/Å	β/°
TaOx/CNF–S250	6.22	3.64	3.88	4.45	–	–	–	–
TaOx/CNF–S400	6.23	3.63	3.85	–	–	–	–	–
TaOx/CNF	6.25	3.63	3.87	4.44	3.86	3.95	3.87	90.3
ICDD value	*6.20*	*3.66*	*3.89*	*4.43*	*3.89*	*3.89*	*3.89*	*90.3*

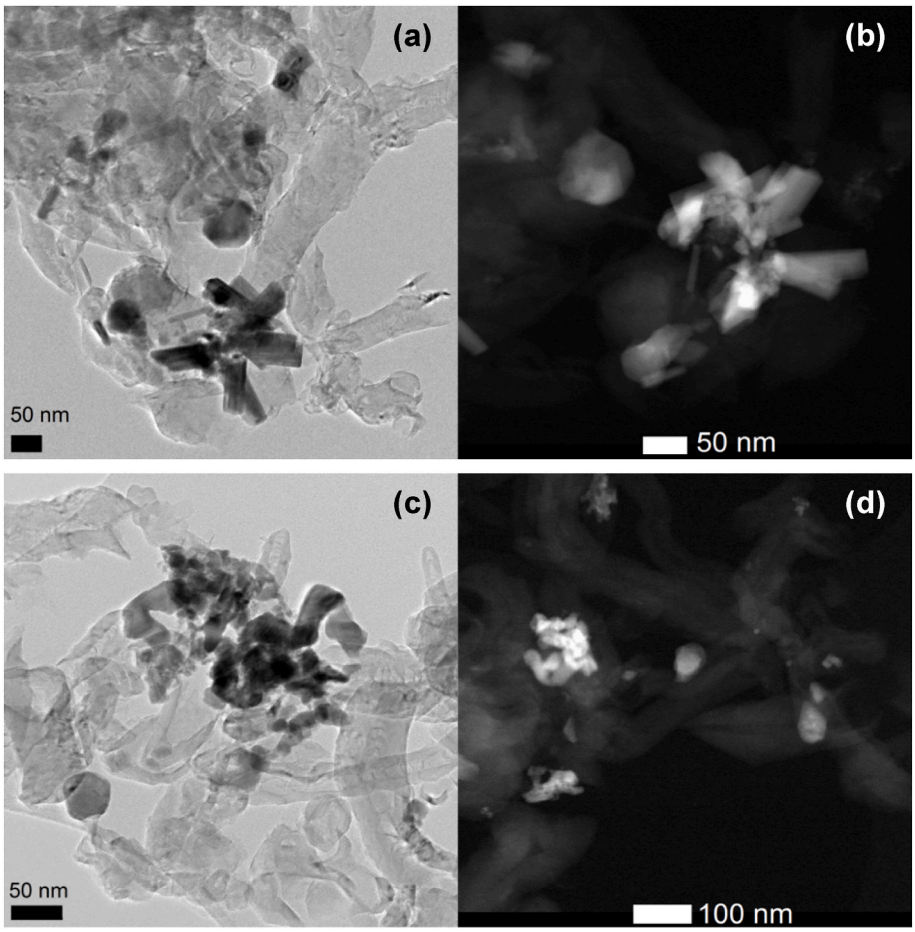

Fig. 4. Representative TEM and STEM images of (a) and (b) TaOx/CNF–S250; and (c) and (d) TaOx/CNF–S400.

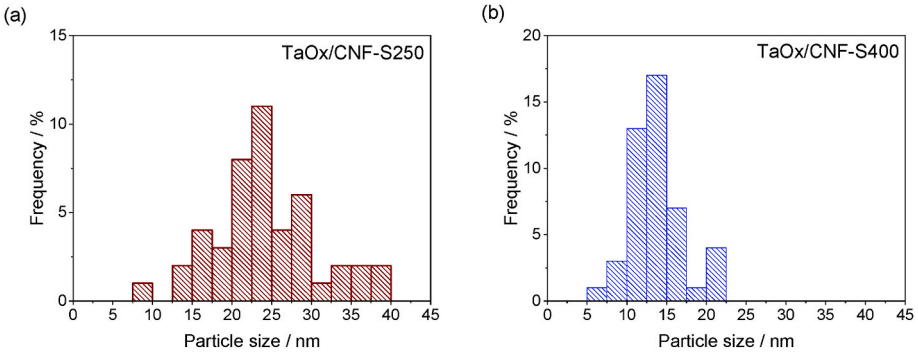

Fig. 5. Particle size distribution of tantalum oxides in (a) TaOx/CNF–S250 and (b) TaOx/CNF–S400 obtained from the analysis of TEM images.

differences among the evaluated catalysts, which indicate a similar reaction mechanism in terms of the number of electrons. Most probably, the tantalum-based catalysts present a balanced mix of active sites towards both $2e^-$ and $4e^-$ (or $2x2e^-$) pathways, which does not change with sulfur doping of the support.

The most relevant electrochemical parameters related to ORR are collected in Table 6. The equivalent data for the experiments with only the supports are summarized in Table S4. The kinetic current density at 0.6 V vs. RHE is significantly higher (2.3 and 3.2 mA cm^{-2}) for the two sulfur-doped CNF-supported catalysts than for the undoped TaOx/CNF (1.4 mA cm^{-2}). In line with the previous description of results, the overpotential ($\eta_{iR\text{-}free}$) at −1 mA cm^{-2} decreases around 50 mV upon sulfur doping of the CNF support. Also the onset potential is 70 mV more positive for the doped materials. All these indicators point to the positive effect of sulfur doping in this class of catalysts. Still, despite presenting proper stability, the tantalum-based catalysts presented herein are not as active as other published catalysts in terms of activity. For example, when combining sodium tantalate ($Na_2Ta_8O_{21}$) with tantalum oxide (Ta_2O_5) and tantalum nitride (Ta_3N_5), the ORR activity is much higher (E_{onset} = 0.9 V vs. RHE in 0.1 M KOH) [40]. Compared to bifunctional catalysts, titanium oxide (another group 4 metal) combined with N-doped graphene [7], or some other combinations of metal oxides (Fe, Co, Ni) with carbon nanofilaments (nanofibers, nanotubes) [23,26,42], present much better ORR activity (E_{onset} above 0.9 V vs. RHE in alkaline conditions), which is closer to benchmark commercial Pt/C catalyst (E_{onset} = 1.01 V vs. RHE [7]). In any case, the results of this work offer a

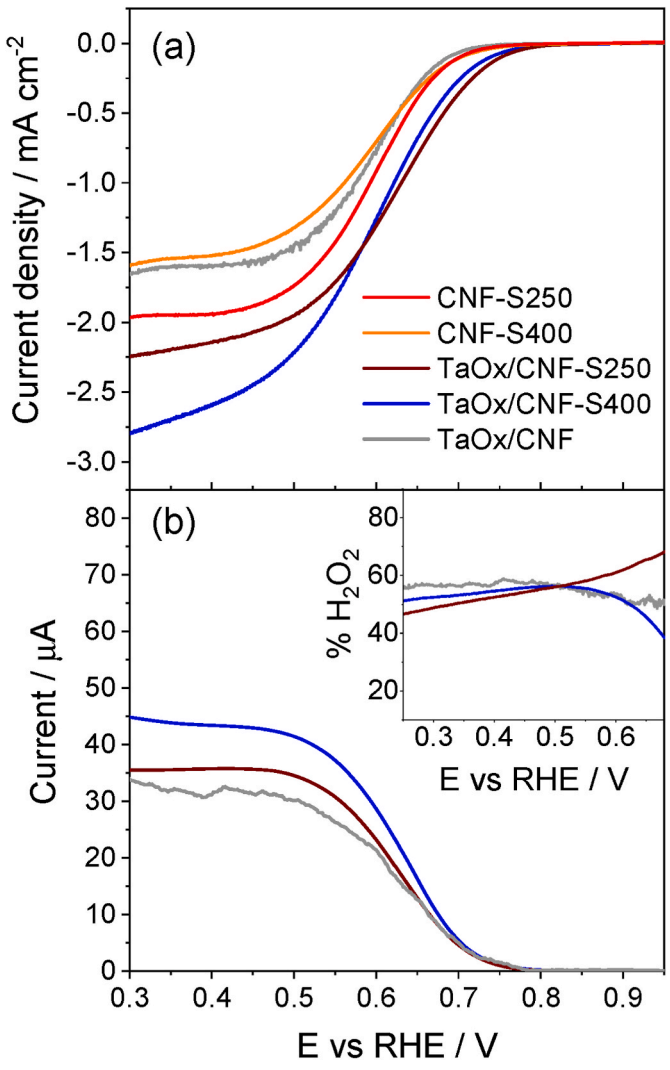

Fig. 6. ORR activity by linear sweep voltammetry at 5 mV s^{-1}, 1600 rpm in 0.1 M NaOH. a) Disk current density; b) ring current at 1.2 V vs. RHE (inset: hydrogen peroxide from ring and disk current results).

new perspective of ORR improvement by means of sulfur doping of carbon supports.

Tafel plots are shown in Fig. 7. At low overpotential, TaOx/CNF–S250 showed a Tafel slope of 70 mV dec^{-1} whilst TaOx/CNF–S400 and TaOx/CNF a Tafel slope of 76 mV dec^{-1}. Considering an associative mechanism for ORR in alkaline medium and the theoretical simulation of Shinagawa et al. [43], a Tafel slope close to 60 mV dec^{-1} indicates that the hydrolysis of adsorbed oxygen is the rate determining step, whilst values closer to 120 mV dec^{-1} are related to the first electron transfer to adsorbed oxygen contributing to the overall reaction rate. The latter takes place at higher overpotential values, as indicated in Fig. 7. Although S-doping affects slightly to the Tafel slope, indicating that the overall reaction mechanism is not very much influenced. However, the exchange current density (j_0) is positively influenced by S-doping (about two orders of magnitude higher), which explains the better behavior compared to undoped catalyst.

3.2.2. OER Electro-activity of S-doped CNF-supported Ta-based catalysts

The OER electrocatalytic activity of the investigated electrocatalysts (polarization curves) together with the ring current is reported in Fig. 8. The rotating speed for the electrode was maintained at 1600 rpm to favor the removal of O_2 bubbles from the electrode surface. There is not iR-correction applied to the OER data. By comparison of supports themselves and TaOx catalysts, the incorporation of tantalum oxides clearly contributes to the enhancement of OER activity, confirming the main conclusions derived from our previous work on undoped CNF as supports [34].

On the other hand, the doping of the support with sulfur does not appear to have a positive influence in OER as it does for the ORR since a slightly lower current density is observed. The ring current in Fig. 8b accounts for the oxygen evolved at the disk, which is reduced at the Pt ring. The trend is similar to that obtained of the disk current, with oxygen efficiencies slightly lower for the S-doped catalysts. The main electrochemical parameters obtained for the OER are collected in Table 7, while those for the supports without Ta-phases are found in Table S5. The two S-doped TaOx/CNF catalysts have less OER activity than the TaOx/CNF in terms of current at a fixed potential ($j_{1.65\ V\ vs\ RHE}$) or overpotential (η), with exception of TaOx/CNF–S250 at low current density. By comparing the two doped samples, the one treated at 250 °C presents a better OER activity as reflected by its lower overpotential and higher current density, although the oxygen efficiency is higher for the catalyst doped at 400 °C. Compared to a benchmark commercial IrO_2 catalyst (η = 370 mV at 10 mA cm^{-2} [7]), the TaOx catalysts present between only 35 and 120 mV higher overpotential.

Tafel plots were used to determine the OER rate determining step

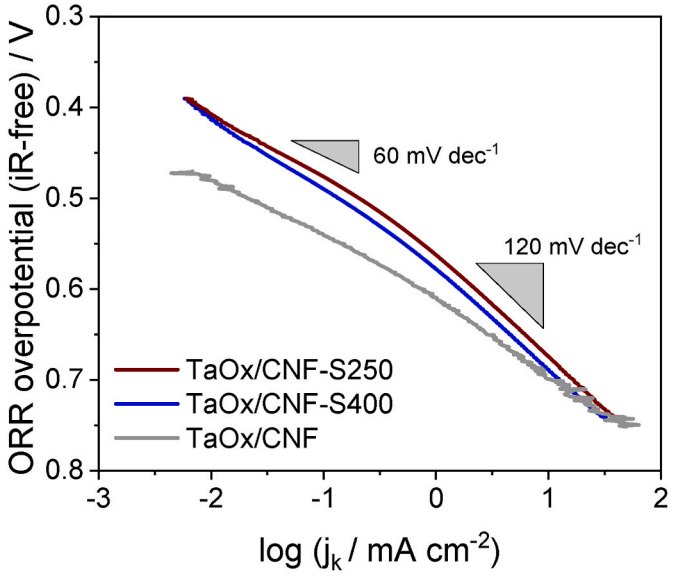

Fig. 7. Tafel plots of S-doped and undoped TaOx/CNF catalysts for the ORR from linear sweep voltammetry experiments at 5 mV s^{-1}, 1600 rpm in 0.1 M NaOH. Tafel slopes of 60 and 120 mV dec^{-1} are indicated as reference.

Table 6
ORR electro-kinetic parameters: onset potential at −0.1 mA cm^{-2} (E_{onset}), Tafel slope (b), exchange current density (j_0), kinetic current density at 0.60 V vs. RHE (absolute value, $j_{k,0.6\ V}$) and iR-corrected overpotential ($\eta_{iR\text{-}free}$), at −1 mA cm^{-2}.

Catalyst	E_{onset} (V vs RHE)	Tafel slope (mV dec^{-1})	$\lvert j_0 \rvert$ (mA cm^{-2})	$\lvert j_{k,0.6\ V} \rvert$ (mA cm^{-2})	$\eta_{iR\text{-}free,\ -1\ mA\ cm^{-2}}$ (mV)
TaOx/CNF–S250	0.75	70	$1.5{\cdot}10^{-8}$	3.2	592
TaOx/CNF–S400	0.75	76	$3.6{\cdot}10^{-8}$	2.3	600
TaOx/CNF	0.74	61	$1.6{\cdot}10^{-10}$	1.4	648

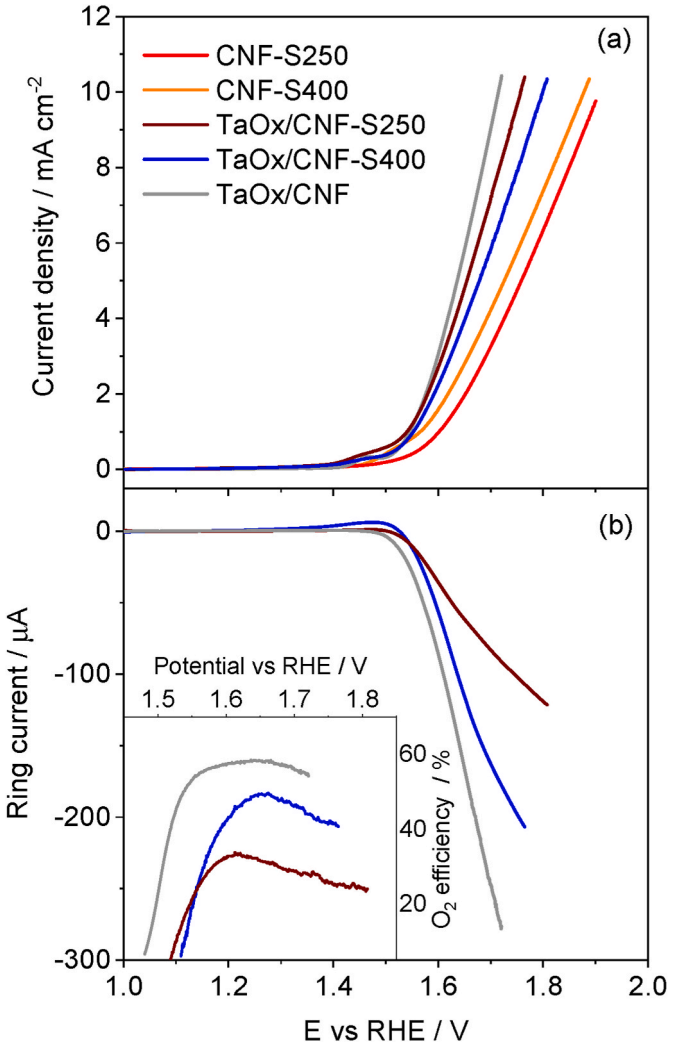

Fig. 8. OER polarization curves by linear sweep voltammetry at 5 mV s^{-1}, 1600 rpm in 0.1 M NaOH. (a) Disk current density; (b) Ring current (inset: oxygen efficiency).

(*rds*) for every catalyst, as presented in Fig. 9. Sulfur-doped catalysts exhibit a Tafel slope slightly over 100 mV dec^{-1}, whilst TaOx/CNF has a lower Tafel slope of 72 mV dec^{-1}. This indicates a clear change of reaction mechanism related to the doping of the support. A Tafel slope of 120 mV dec^{-1} appears when the surface species formed in the step just before the rate-determing step is predominant. In other cases, the Tafel slope is lower than 120 mV dec^{-1} for the overpotential values evaluated in Fig. 9. An intermediate value of 100 mV dec^{-1} is thus the result from a mixture of active species, with some of them favoring the pathway related to a Tafel slope of 60 mV dec^{-1} (the preferential adsorption of reaction intermediates is the *rds*) and some other acting with a Tafel slope of 120 mV dec^{-1} (the *rds* is the formation of hydroxide) [43].

3.2.3. Endurance tests and bifunctionality

The different catalysts were investigated under a chronopotentiometric test in order to determine the electrode stability with time under ORR and OER conditions. Fig. 10a and b show the variation of the potential with the number of cycles for OER and ORR, respectively. The test consisted of consecutive cycles of OER/ORR, implementing currents of +1 mA cm^{-2} and -1 mA cm^{-2}. A duration of 3 min for sequence was programmed with cut-off potential values of 0.2 V and 1.9 V vs. RHE. In OER, the potential is quite stable with time, indicating a good stability of the set of catalysts for this reaction regardless the support used. Whereas, in ORR there is a decrease of potential in the first 10–15 cycles of approximately 50–60 mV with a much slower loss in the next ones. TaOx/CNF shows a sharp decrease of potential in ORR which is recovered after 10 cycles, indicating a reversible loss at the beginning of the experiment. Based on these results, it appears that the TaOx catalysts suffer some deactivation in ORR but good stability in OER. Upon cycling, the active sites responsible for ORR loss partial activity which does not affect OER behavior. It occurs for the three catalysts, independently of the support used. This phenomenon points to the presence of different active sites for both reactions, which is in line with other bifunctional catalysts with multiactive centers.

To sum up, Fig. 10c includes the values of overpotential for both ORR and OER for the different formulations, considering both polarization curves and chronopotentiometric experiments. The sum of ORR and OER overpotentials accounts for the reversibility of catalysts defined as $\Delta E = E_{OER} - E_{ORR} = \eta_{OER} + \eta_{ORR}$. The sulfur doping of the CNF leads to a significant improvement of ΔE from 970 mV to 905 mV in the polarization curves, and from 1100 mV to 1020 mV in chronopotentiometric experiments. This is an enhancement of up to 80 mV, i.e. considering both ORR and OER, mostly coming from the better behavior for the oxygen reduction. This enhancement is maintained upon endurance tests, with particular better results for the catalyst doped at 400 °C. This particular catalyst presents a lower particle size for Ta oxides and lower

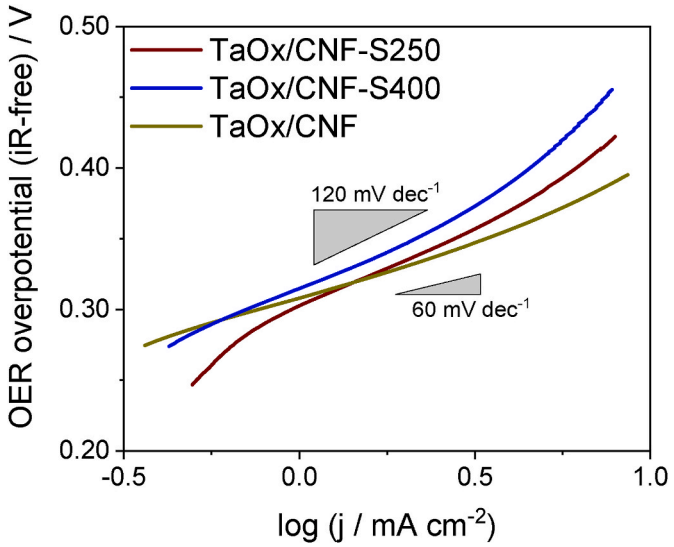

Fig. 9. Tafel plots of TaOx/CNF and TaOx/CNF–S catalysts for the OER from linear sweep voltammetry experiments at 5 mV s^{-1}, 1600 rpm in 0.1 M NaOH. Tafel slopes of 60 and 120 mV dec^{-1} are indicated as reference.

Table 7
OER electro-kinetic parameters: onset potential (E_{onset}), Tafel slope (b), exchange current density (j_0), current density at 1.65 V vs. RHE, and iR-corrected overpotential (η) at 1 and 10 mA cm^{-2}.

Catalyst	E_{onset} (V vs RHE)	Tafel slope (mV dec^{-1})	j_0 (mA cm^{-2})	$j_{1.65\ V\ vs\ RHE}$ (mA cm^{-2})	$\eta_{iR\text{-}free,\ 10\ mA\ cm^{-2}}$ (mV)	$\eta_{iR\text{-}free,\ 1\ mA\ cm^{-2}}$ (mV)
TaOx/CNF–S250	1.47	109	$1.6{\cdot}10^{-3}$	4.8	446	302
TaOx/CNF–S400	1.48	105	$1.3{\cdot}10^{-3}$	4.0	489	314
TaOx/CNF	1.48	72	$5.1{\cdot}10^{-5}$	5.8	405	308

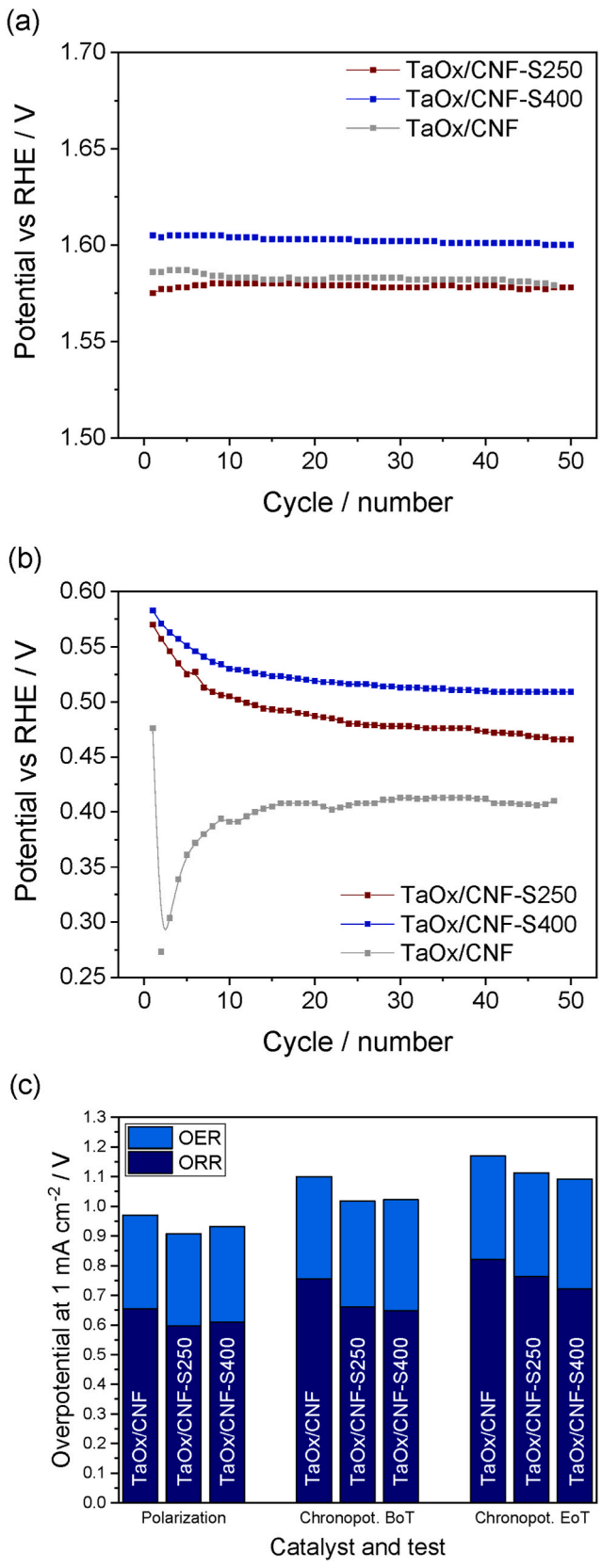

Fig. 10. Potential variation along successive chronopotentiometric square cycles at 1 mA cm^{-2} (400 rpm) for (a) OER and (b) ORR. (c) Overpotential values according to catalyst and test: polarization curves (1600 rpm) or chronopotentiometric experiments, at the beginning and at the end of test (BoT/EoT). All data are registered in O_2-saturated 0.1 M NaOH.

O/Ta ratio than its S-doped counterpart treated at 250 °C as main differences, which supports the hypothesis of substoichiometry and low particle size conditioning the electrocatalytic behavior. The reversibility of published bifunctional catalysts in terms of ΔE is variable and its determination depends on the electrolyte used and the criteria for calculation. For example, Luque-Centeno et al. reported ΔE of 846 mV for a catalyst based on titanium supported on N-doped graphene, at 5 mA cm^{-2} in 0.1 M NaOH [7]. Other transition metal-based bifuncional catalysts from the state of the art exhibit ΔE values above 800 mV (spinels or metals combined with N-doped carbons) or above 900 mV (perovskites), with nanocomposites presenting the best bifunctional behavior with ΔE in the range 700–800 mV, similar to the best noble metal combinations [44–46].

To sum up, the work described herein presents an alternative strategy to improve the activity and durability of oxygen bifunctional catalysts by sulfur doping of highly resistant carbon nanofibers and using a durable active phase like tantalum oxide. More work is needed to further increase the activity towards the current state of the art noble metals.

4. Conclusions

In summary, we have studied new sulfur-doped CNF-supported tantalum based catalysts with bifunctional characteristics for the ORR/OER in alkaline media. The combination of high temperature and short time (400 °C for 3 h) and lower temperature for longer time (250 °C for 6 h) have been evaluated over CNF grown at 700 °C. Sulfur doping has been successful on both supports. The combination of tantalum oxide and S-doped CNF has been tested to determine the bifunctional activity of these new materials. The support doping improved the activity of the catalysts, in particular on the oxygen reduction reaction. However, the difference in activity between the doped materials is not enough remarkable to determine the effect of each doping procedure on the overall activity of the catalyst. These new materials have interesting bifunctional activity both for the ORR and OER, being slightly better for TaOx/CNF–S250. TaOx/CNF–S new catalysts also show good stability through time, especially for the OER. Future studies will be focused on improving the OER activity preserving the interesting bifunctionality of TaOx/CNF–S electrocatalysts.

CRediT authorship contribution statement

Juan Carlos Ruiz-Cornejo: Methodology, Investigation, Data curation, Formal analysis, Writing – original draft. **David Sebastián:** Conceptualization, Methodology, Validation, Resources, Writing – review & editing, Visualization. **Juan Ignacio Pardo:** Validation, Writing – review & editing. **María Victoria Martínez-Huerta:** Supervision, Funding acquisition, Writing – review & editing. **María Jesús Lázaro:** Supervision, Project administration, Funding acquisition.

Declaration of competing interest

The authors declare that they have no known competing financial interests or personal relationships that could have appeared to influence the work reported in this paper.

Data availability

Data will be made available on request.

Acknowledgements

The authors wish to acknowledge the grants PID2020-115848RB-C21 and PID2020-115848RB-C22 funded by MCIN/AEI/10.13039/501100011033, and to the *Gobierno de Aragón* (DGA) for the funding to *Grupo de Conversión de Combustibles* (T06_17R). J.C. Ruiz-Cornejo acknowledges also DGA for his PhD grant.

Appendix A. Supplementary data

Supplementary data to this article can be found online at https://doi.org/10.1016/j.jpowsour.2022.231988.

References

[1] J.W. Desmond Ng, Y. Gorlin, T. Hatsukade, T.F. Jaramillo, A precious-metal-free regenerative fuel cell for storing renewable electricity, Adv. Energy Mater. 3 (2013) 1545–1550, https://doi.org/10.1002/aenm.201300492.

[2] L. Zong, W. Wu, S. Liu, H. Yin, Y. Chen, C. Liu, K. Fan, X. Zhao, X. Chen, F. Wang, Y. Yang, L. Wang, S. Feng, Metal-free, active nitrogen-enriched, efficient bifunctional oxygen electrocatalyst for ultrastable zinc-air batteries, Energy Storage Mater. 27 (2020) 514–521, https://doi.org/10.1016/j.ensm.2019.12.013.

[3] K. Zeng, X. Zheng, C. Li, J. Yan, J. Tian, C. Jin, P. Strasser, R. Yang, Recent advances in non-noble bifunctional oxygen electrocatalysts toward large-scale production, Adv. Funct. Mater. 30 (2020), 2000503, https://doi.org/10.1002/adfm.202000503.

[4] A. Kraytsberg, Y. Ein-Eli, Review on Li-air batteries - opportunities, limitations and perspective, J. Power Sources 196 (2011) 886–893, https://doi.org/10.1016/j.jpowsour.2010.09.031.

[5] L. Dong, R.R.S. Gari, Z. Li, M.M. Craig, S. Hou, Graphene-supported platinum and platinum–ruthenium nanoparticles with high electrocatalytic activity for methanol and ethanol oxidation, Carbon N. Y. 48 (2010) 781–787, https://doi.org/10.1016/j.carbon.2009.10.027.

[6] A.M. El-Sawy, I.M. Mosa, D. Su, C.J. Guild, S. Khalid, R. Joesten, J.F. Rusling, S. L. Suib, Controlling the active sites of sulfur-doped carbon nanotube-graphene nanolobes for highly efficient oxygen evolution and reduction catalysis, Adv. Energy Mater. 6 (2016), 1501966, https://doi.org/10.1002/aenm.201501966.

[7] J.M. Luque-Centeno, M.V. Martínez-Huerta, D. Sebastián, S. Pérez-Rodríguez, M. J. Lázaro, Titanium dioxide/N-doped graphene composites as non-noble bifunctional oxygen electrocatalysts, Ind. Eng. Chem. Res. 60 (51) (2021) 18817–18830, https://doi.org/10.1021/acs.iecr.1c02896.

[8] X. Wang, X. Zhang, G. Fu, Y. Tang, Recent progress of electrospun porous carbon-based nanofibers for oxygen electrocatalysis, Mater, Today Energy 22 (2021), 100850, https://doi.org/10.1016/j.mtener.2021.100850.

[9] J.C. Ruiz-Cornejo, D. Sebastián, M.J. Lázaro, Synthesis and applications of carbon nanofibers: a review, Rev. Chem. Eng. 36 (2020) 493–511, https://doi.org/10.1515/revce-2018-0021.

[10] D. Sebastián, M.J.J. Lázaro, R. Moliner, I. Suelves, A.S.S. Aricò, V. Baglio, Oxidized carbon nanofibers supporting PtRu nanoparticles for direct methanol fuel cells, Int. J. Hydrogen Energy 39 (2014) 5414–5423, https://doi.org/10.1016/j.ijhydene.2013.12.005.

[11] C. Li, Z. Zhang, M. Wu, R. Liu, FeCoNi ternary alloy embedded mesoporous carbon nanofiber: an efficient oxygen evolution catalyst for rechargeable zinc-air battery, Mater. Lett. 238 (2019) 138–142, https://doi.org/10.1016/j.matlet.2018.11.160.

[12] T. Li, Y. Lv, J. Su, Y. Wang, Q. Yang, Y. Zhang, J. Zhou, L. Xu, D. Sun, Y. Tang, Anchoring CoFe2O4 nanoparticles on N-doped carbon nanofibers for high-performance oxygen evolution reaction, Adv. Sci. 4 (2017), https://doi.org/10.1002/advs.201700226.

[13] Z.K. Ghouri, N.A.M. Barakat, M. Obaid, J.H. Lee, H.Y. Kim, Co/CeO_2-decorated carbon nanofibers as effective non-precious electro-catalyst for fuel cells application in alkaline medium, Ceram. Int. 41 (2015) 2271–2278, https://doi.org/10.1016/j.ceramint.2014.10.031.

[14] Y.P. Zhu, Y. Jing, A. Vasileff, T. Heine, S.Z. Qiao, 3D synergistically active carbon nanofibers for improved oxygen evolution, Adv. Energy Mater. 7 (2017), 1602928, https://doi.org/10.1002/aenm.201602928.

[15] J.M. Luque-Centeno, M.V. Martínez-Huerta, D. Sebastián, G. Lemes, E. Pastor, M. J. Lázaro, Bifunctional N-doped graphene Ti and Co nanocomposites for the oxygen reduction and evolution reactions, Renew. Energy 125 (2018) 182–192, https://doi.org/10.1016/j.renene.2018.02.073.

[16] M. Li, L. Zhang, Q. Xu, J. Niu, Z. Xia, N-doped graphene as catalysts for oxygen reduction and oxygen evolution reactions: theoretical considerations, J. Catal. 314 (2014), https://doi.org/10.1016/j.jcat.2014.03.011.

[17] Z. Li, B. Li, C. Yang, S. Lin, Q. Pang, P. Shen, Controllable preparation of nitrogen-doped graphitized carbon from molecular precursor as non-metal oxygen evolution reaction electrocatalyst, Appl. Surf. Sci. 491 (2019) 723–734, https://doi.org/10.1016/j.apsusc.2019.06.183.

[18] J. Quílez-Bermejo, E. Morallón, D. Cazorla-Amorós, Metal-free heteroatom-doped carbon-based catalysts for ORR. A critical assessment about the role of heteroatoms, Carbon N. Y. 165 (2020) 434–454, https://doi.org/10.1016/j.carbon.2020.04.068.

[19] S.R. Ede, Z. Luo, Tuning the intrinsic catalytic activities of oxygen-evolution catalysts by doping: a comprehensive review, J. Mater. Chem. A. 9 (2021) 20131–20163, https://doi.org/10.1039/d1ta04032d.

[20] Z. Moosapour Siahkalroudi, B. Aghabarari, M. Vaezi, E. Rodríguez-Castellón, M. V. Martínez-Huerta, Effect of secondary heteroatom (S, P) in N-doped reduced graphene oxide catalysts to oxygen reduction reaction, Mol. Catal. 502 (2021), https://doi.org/10.1016/j.mcat.2020.111372.

[21] R. Hu, Y. Li, Q. Zeng, J. Shang, Role of active sites in N-coordinated Fe-Co dual-metal doped graphene for oxygen reduction and evolution reactions: a theoretical insight, Appl. Surf. Sci. 525 (2020), https://doi.org/10.1016/j.apsusc.2020.146588.

[22] D.I. Jeong, H.W. Choi, S. Woo, J.H. Yoo, M. Kumar, Y.H. Song, B. Lim, B.K. Koo, B. K. Kang, D.H. Yoon, Complementary performance improved crystalline N-doped carbon encapsulated CoFe/mesoporous N-doped graphene foam as bifunctional catalyst, Appl. Surf. Sci. 559 (2021), https://doi.org/10.1016/j.apsusc.2021.149077.

[23] C. Alegre, C. Busacca, A. Di Blasi, O. Di Blasi, A.S. Aricò, V. Antonucci, V. Baglio, Toward more efficient and stable bifunctional electrocatalysts for oxygen electrodes using $FeCo_2O_4$/carbon nanofiber prepared by electrospinning, Mater. Today Energy 18 (2020), https://doi.org/10.1016/j.mtener.2020.100508.

[24] C. Alegre, C. Busacca, A. Di Blasi, O. Di Blasi, A.S. Aricò, V. Antonucci, V. Baglio, Electrocatalysis of oxygen on bifunctional nickel-cobaltite spinel, Chemelectrochem 7 (2020) 124–130, https://doi.org/10.1002/celc.201901584.

[25] C. Alegre, C. Busacca, A. Di Blasi, O. Di Blasi, A.S. Aricò, V. Antonucci, E. Modica, V. Baglio, Electrospun carbon nanofibers loaded with spinel-type cobalt oxide as bifunctional catalysts for enhanced oxygen electrocatalysis, J. Energy Storage 23 (2019) 269–277, https://doi.org/10.1016/j.est.2019.04.001.

[26] C. Alegre, E. Modica, A. Di Blasi, O. Di Blasi, C. Busacca, M. Ferraro, A.S. Aricò, V. Antonucci, V. Baglio, NiCo-loaded carbon nanofibers obtained by electrospinning: bifunctional behavior as air electrodes, Renew. Energy 125 (2018) 250–259, https://doi.org/10.1016/j.renene.2018.02.089.

[27] D. Higgins, M.A. Hoque, M.H. Seo, R. Wang, F. Hassan, J.-Y. Choi, M. Pritzker, A. Yu, J. Zhang, Z. Chen, Development and simulation of sulfur-doped graphene supported platinum with exemplary stability and activity towards oxygen reduction, Adv. Funct. Mater. 24 (2014) 4325–4336, https://doi.org/10.1002/adfm.201400161.

[28] M.A. Hoque, F.M. Hassan, M.H. Seo, J.Y. Choi, M. Pritzker, S. Knights, S. Ye, Z. Chen, Optimization of sulfur-doped graphene as an emerging platinum nanowires support for oxygen reduction reaction, Nano Energy 19 (2016) 27–38, https://doi.org/10.1016/j.nanoen.2015.11.004.

[29] M.A. Hoque, F.M. Hassan, D. Higgins, J.Y. Choi, M. Pritzker, S. Knights, S. Ye, Z. Chen, Multigrain platinum nanowires consisting of oriented nanoparticles anchored on sulfur-doped graphene as a highly active and durable oxygen reduction electrocatalyst, Adv. Mater. 27 (2015) 1229–1234, https://doi.org/10.1002/adma.201404426.

[30] O.L. Li, Z. Shi, H. Lee, T. Ishizaki, Enhanced electrocatalytic stability of platinum nanoparticles supported on sulfur-doped carbon using in-situ solution plasma, Sci. Rep. 9 (2019) 1–10, https://doi.org/10.1038/s41598-019-49194-x.

[31] X. Xing, R. Liu, M. Anjass, K. Cao, U. Kaiser, G. Zhang, C. Streb, Bimetallic manganese-vanadium functionalized N,S-doped carbon nanotubes as efficient oxygen evolution and oxygen reduction electrocatalysts, Appl. Catal. B Environ. 277 (2020), 119195, https://doi.org/10.1016/j.apcatb.2020.119195.

[32] Y. Gao, H. Zhao, D. Chen, C. Chen, F. Ciucci, In situ synthesis of mesoporous manganese oxide/sulfur-doped graphitized carbon as a bifunctional catalyst for oxygen evolution/reduction reactions, Carbon N. Y. 94 (2015) 1028–1036, https://doi.org/10.1016/j.carbon.2015.07.084.

[33] J.C. Ruiz-Cornejo, D. Sebastián, M.V. Martínez-Huerta, M.J. Lázaro, Tantalum-based electrocatalysts prepared by a microemulsion method for the oxygen reduction and evolution reactions, Electrochim. Acta 317 (2019) 261–271, https://doi.org/10.1016/j.electacta.2019.05.145.

[34] J.C. Ruiz-Cornejo, J.F. Vivo-Vilches, D. Sebastián, M.V. Martínez-Huerta, M. J. Lázaro, Carbon nanofiber-supported tantalum oxides as durable catalyst for the oxygen evolution reaction in alkaline media, Renew. Energy 178 (2021) 307–317, https://doi.org/10.1016/j.renene.2021.06.076.

[35] I. Suelves, M.J. Lázaro, R. Moliner, Y. Echegoyen, J.M. Palacios, Characterization of NiAl and NiCuAl catalysts prepared by different methods for hydrogen production by thermo catalytic decomposition of methane, Catal. Today 116 (2006) 271–280, https://doi.org/10.1016/j.cattod.2006.05.071.

[36] M.H. Oh, N. Lee, H. Kim, S.P. Park, Y. Piao, J. Lee, S.W. Jun, W.K. Moon, S.H. Choi, T. Hyeon, Large-scale synthesis of bioinert tantalum oxide nanoparticles for X-ray computed tomography imaging and bimodal image-guided sentinel lymph node mapping, J. Am. Chem. Soc. 133 (2011) 5508–5515, https://doi.org/10.1021/ja200120k.

[37] A. Ishihara, S. Tominaka, S. Mitsushima, H. Imai, O. Sugino, K. Ota, Challenge of advanced low temperature fuel cells based on high degree of freedom of group 4 and 5 metal oxides, Curr. Opin. Electrochem. 21 (2020) 234–241, https://doi.org/10.1016/j.coelec.2020.03.005.

[38] W. Kiciński, M. Szala, M. Bystrzejewski, Sulfur-doped porous carbons: synthesis and applications, Carbon N. Y. 68 (2014) 1–32, https://doi.org/10.1016/j.carbon.2013.11.004.

[39] N. Benito, C. Palacio, Nanostructuring of Ta_2O_5 surfaces by low energy Ar^+ bombardment, Appl. Surf. Sci. 351 (2015) 753–759, https://doi.org/10.1016/j.apsusc.2015.05.143.

[40] G. Zhang, D. Sebastián, X. Zhang, Q. Wei, C. Lo Vecchio, J. Zhang, V. Baglio, W. Wang, S. Sun, A.S. Aricò, A.C. Tavares, Engineering of a low-cost, highly active, and durable tantalate–graphene hybrid electrocatalyst for oxygen reduction, Adv. Energy Mater. (2020) 1–11, https://doi.org/10.1002/aenm.202000075, 2000075.

[41] D. Sebastián, V. Baglio, S. Sun, A.C. Tavares, A.S. Aricò, Graphene-supported substoichiometric sodium tantalate as a methanol-tolerant, non-noble-metal catalyst for the electroreduction of oxygen, ChemCatChem 7 (2015) 911–915, https://doi.org/10.1002/cctc.201403026.

[42] X. Xiao, X. Li, G. Yu, J. Wang, G. Yan, Z. Wang, H. Guo, FeCox alloy nanoparticles encapsulated in three-dimensionally N-doped porous carbon/multiwalled carbon nanotubes composites as bifunctional electrocatalyst for zinc-air battery, J. Power Sources 438 (2019), 227019, https://doi.org/10.1016/j.jpowsour.2019.227019.

[43] T. Shinagawa, A.T. Garcia-Esparza, K. Takanabe, Insight on Tafel slopes from a microkinetic analysis of aqueous electrocatalysis for energy conversion, Sci. Rep. 5 (2015) 1–21, https://doi.org/10.1038/srep13801.
[44] X. Wu, C. Tang, Y. Cheng, X. Min, S.P. Jiang, S. Wang, Bifunctional catalysts for reversible oxygen evolution reaction and oxygen reduction reaction, Chem. Eur J. 26 (2020) 3906–3929, https://doi.org/10.1002/chem.201905346.
[45] Y.L. Zhang, K. Goh, L. Zhao, X.L. Sui, X.F. Gong, J.J. Cai, Q.Y. Zhou, H. Da Zhang, L. Li, F.R. Kong, D.M. Gu, Z.B. Wang, Advanced non-noble materials in bifunctional catalysts for ORR and OER toward aqueous metal-air batteries, Nanoscale 12 (2020) 21534–21559, https://doi.org/10.1039/d0nr05511e.
[46] S.S. Sekhon, J. Lee, J.S. Park, Biomass-derived bifunctional electrocatalysts for oxygen reduction and evolution reaction: a review, J. Energy Chem. 65 (2021) 149–172, https://doi.org/10.1016/j.jechem.2021.05.052.